

# Effective band-projected description of interacting quasiperiodic systems

Flavio Riche,<sup>1</sup> Raul Liquito,<sup>2</sup> Bruno Amorim,<sup>3,4</sup> Eduardo V. Castro,<sup>2,5</sup> Pedro Ribeiro,<sup>1,5</sup> and Miguel Gonçalves<sup>6</sup>

<sup>1</sup>*CeFEMA-LaPMET, Physics Department, Instituto Superior Técnico, Universidade de Lisboa, Av. Rovisco Pais, 1049-001 Lisboa, Portugal*

<sup>2</sup>*Centro de Física das Universidades do Minho e Porto, LaPMET, Departamento de Física e Astronomia, Faculdade de Ciências, Universidade do Porto, 4169-007 Porto, Portugal*

<sup>3</sup>*Centro de Física das Universidades do Minho e Porto, LaPMET, Universidade do Minho, Campus of Gualtar, 4710-057, Braga, Portugal*

<sup>4</sup>*International Iberian Nanotechnology Laboratory (INL), Av. Mestre José Veiga, 4715-330 Braga, Portugal*

<sup>5</sup>*Beijing Computational Science Research Center, Beijing 100084, China*

<sup>6</sup>*Princeton Center for Theoretical Science, Princeton University, Princeton, NJ 08544*

We study the interplay between electronic interactions and quasiperiodicity in a one-dimensional narrow-band system, focusing on ground-state and low-energy excitation properties. Using band projection as a low-energy effective approach, we show that a projection restricted to first order in the interaction strength fails to reproduce the correlated phase diagram. This contrasts with the standard success of first-order band projection in translationally invariant flat-band systems and highlights the essential role of virtual processes involving remote bands in quasiperiodic settings. By incorporating second-order interband contributions perturbatively, we obtain an effective Hamiltonian that quantitatively reproduces the exact phase diagram previously obtained using density matrix renormalization group calculations, including the transition between a Luttinger liquid and a charge-density-wave phase and the crossover to a quasifractal charge-density-wave regime at strong quasiperiodicity. We further use this controlled framework to investigate low-energy neutral excitations and the optical conductivity, identifying clear dynamical signatures distinguishing the different phases. Our results establish second-order band projection as a reliable tool for correlated quasiperiodic narrow-band systems and suggest a promising route for studying interacting quasiperiodic and moiré materials beyond one dimension.

## I. INTRODUCTION

Quasiperiodic structures can differ fundamentally from periodic crystalline structures. Incommensurability subtly breaks translational symmetry in an intrinsic way, leaving long-range correlations between lattice sites, whose significance has long been recognized in one-dimensional (1D) systems.

In 1D, quasiperiodicity can dramatically change the electronic properties relative to the crystalline case, allowing for extended, localized [1–7] or multifractal [8–13] wave functions. This fundamentally contrasts with the effects of disorder, that generically localizes the wave function in 1D. The Aubry-André (AA) model [1] is the simplest example of a 1D quasiperiodic system that describes a quasiperiodicity-induced transition between an extended and a localized phase. This model can be experimentally realized by in different platforms, including in optical and photonic lattices [5, 11, 14–18]. Generalizations of the AA can give rise to very rich phase diagrams with different localization properties, including critical phases with multifractal eigenstates [10, 11, 19, 20], and mobility edges between extended, localized and critical phases [8, 11, 21–26].

The interplay between quasiperiodicity and interactions is a challenging problem that has had recent important developments in 1D [27–33]. However, the relevance

of this interplay in higher dimensions, and in particular in moiré systems - where quasiperiodicity can also induce non-trivial localization properties at the single-particle level [3, 4, 34] - remains an open question.

In our previous research [28] we showed that quasiperiodicity can be responsible for the emergence of new correlated phases in a 1D narrow-band system, using DMRG to obtain the full exact phase diagram. Extending our analysis to higher-dimensional systems is however significantly more challenging because DMRG and other exact methods such as exact diagonalization are restricted to small system sizes. Additionally, calculating dynamic properties, such as the optical conductivity, becomes particularly challenging with DMRG, even in one dimension, due to the need of capturing excited states. With this motivation, we explore the band projection (BP) technique as a possible route to study interacting quasiperiodic systems, using the model in Ref. [28] as a test bed.

Projection onto flat or narrow bands is an approach that dates back to the study of the fractional quantum Hall effect [35]. More recently, it has become a standard approach to study the low-energy physics of interacting moiré systems [36, 37]. The band projection technique has also been applied to investigate fractional Chern insulators, where the projection of interactions on a topological flatband provides an effective description of emergent fractionalized phases [38–41]. While it is possible to successfully capture experimentally observed corre-

lated phases by projecting the Hamiltonian into a single narrow-band, it is only well justified if the intra-band gap is much larger than all other energy scales. Away from this extreme regime, remote bands can also play an important role [42–50]. Moreover, even if band projection methods have been extensively explored in translationally invariant systems, a comprehensive assessment of their validity and effectiveness when translational symmetry is explicitly broken is currently lacking. Answering these questions is of crucial importance for exploring the physics of moiré systems, where BP could provide a controlled route to incorporating the interplay between quasiperiodicity and interactions exactly.

In this work, we apply the band projection technique in a 1D narrow-band quasiperiodic system, using the model in Ref. [28] as a test bed for quasiperiodic systems. We find that naive projection onto the narrow band fails to reproduce any of the ground-state phase transitions previously obtained with DMRG in a numerically exact manner, whereas perturbatively including remote-band effects up to second order in the interaction strength captures both the transitions between the exact Luttinger liquid (LL) and charge-density-wave (CDW) phases, as well as the exotic quasi-fractal regime found in Ref. [28]. Building on the success of this approach to describe the ground-state phase diagram, we extend our analysis beyond ground-state physics, investigating dynamical properties of the model, with special focus on the optical conductivity.

The paper is structured as follows: Section II outlines the BP method and the physical quantities that we will be studying throughout the manuscript; Section III presents the results for the ground-state phase diagram and low-energy neutral excitations; and section IV summarizes our main findings. Additional results, details on the BP technique and the computation of the optical conductivity are provided in the Appendices.

## II. MODEL AND METHODS

We consider a 1D lattice model of spinless fermions with nearest-neighbor hoppings modulated quasiperiodically [10, 28] and repulsive nearest-neighbor interactions ( $U > 0$ ), given by:

$$H = H_0 + V = - \sum_{r=0}^{N-1} t_r (c_r^\dagger c_{r+1} + H.c.) + U \sum_{r=0}^{N-1} n_r n_{r+1}, \quad (1)$$

where  $H_0$  and  $V$  are respectively the single-particle and interacting parts of the Hamiltonian,  $c_r^\dagger$  is the creation operator at site  $r$ ,  $t_r = 1 + V_2 \cos[2\pi\tau(r + 1/2) + \phi]$  is the nearest-neighbor hopping, with modulation strength  $V_2$  and period  $\tau^{-1}$ ,  $\phi$  is the phase shift and  $U$  is the interaction strength. We implement twisted boundary

conditions through the substitution  $t \rightarrow te^{i\theta/N}$ , where  $\theta$  is the phase twist.

When  $\tau$  is an irrational number, translational symmetry is broken, and the system is quasiperiodic. In order to reduce the finite size effects, we work with rational approximants,  $\tau \simeq \tau_{N',N} = N'/N$ , where  $N$  is the system size, corresponding to a single unit cell. In our work we choose  $\tau = \sqrt{\pi}^{-1} \simeq 0.5642$ , which allows the formation of a nearly flatband (FB) close to  $V_2 = 1$ , as shown in Fig. 1(a), associated with a moiré pattern of length  $L_M = (\tau - 1/2)^{-1}/2 \simeq 7.8$ , shown in Fig. 1(b). It is important to note that because of quasiperiodicity, there is no longer any notion of Bloch bands. However, it is possible to identify in Fig. 1(a) a cluster of states around  $E = 0$ , that we will refer to as a narrow-band or nearly flatband. As  $\tau$  gets closer to  $1/2$ , the band becomes considerably flatter, with an increasing  $L_M$  [10, 28], in which case the effect of interactions is expected to be enhanced.

The non-interacting model ( $U = 0$ ) hosts extended states for  $V_2 < 1$  and critical states for  $V_2 \geq 1$ . Once interactions are turned on, the model displays Luttinger liquid (LL) and charge density wave (CDW) phases. For  $V_2 \geq 1$  there is a crossover between the CDW and a quasifractal-charge density wave (qf-CDW), that develops at smaller  $U$ . In fact, the quasiperiodic-induced critical phase at  $V_2 \geq 1$  is unstable towards the qf-CDW regime at any finite  $U$ . In contrast, when the system is periodic (i.e.  $\tau$  is chosen to be a rational), the small  $U$  phase is a LL. While in a truly fractal-CDW phase the number of ordered wavevectors contributing to the charge modulations would diverge, in the qf-CDW regime the numerical results indicate that the number of wavevectors is finite, although strongly increasing in this regime [28]. The phase diagram in the parameter space of  $V_2$  and  $U$  is schematically shown in Fig. 1(c).

Solving Eq. 1 using full exact diagonalization (ED) is unpractical due to the exponential growth of the Hilbert space, posing significant limitations to accessing the thermodynamic limit. To overcome this challenge, we employ the BP technique.

We work at half-filling in an interaction regime that is strong compared to the width of the narrow band ( $W$ ) and weak compared to the bandgap ( $\Delta$ ),  $W \ll U \ll \Delta$ . For  $V_2 = 0.9$ , we have  $W \simeq 5 \times 10^{-3}$  and  $\Delta \simeq 1.5$ . Throughout the manuscript, we focus on  $U \leq 0.6$ . In this case, the interaction-induced mixing between the FB and the remote bands can be treated perturbatively. In the absence of interband excitations, the states in the lower band can be considered as "frozen", since the band is fully occupied and intraband excitations are Pauli-blocked, while the upper band remains energetically inaccessible and thus completely empty. For this reason, we label such bands as occupied (OC) and empty (E).

We start by defining the band creation and annihilation operators

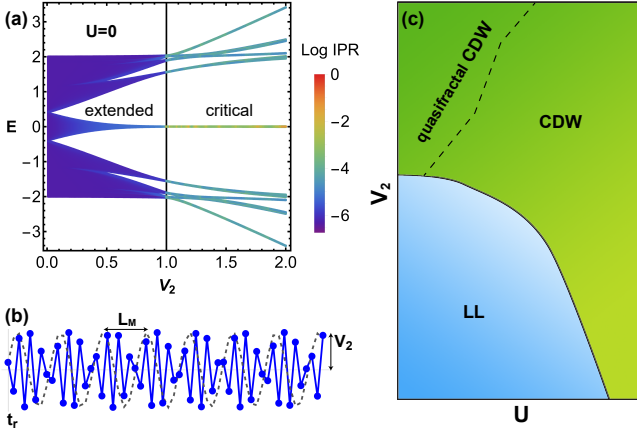


FIG. 1. (a) Single-particle IPR of the model given by Eq. 1 in the non-interacting limit as a function of the quasiperiodic potential strength,  $V_2$ , and energy,  $E$ , for  $L = 842$ ,  $\tau = 475/842$  and  $\phi = 0$ . (b) Hopping modulation of the model, which creates a moiré pattern of length  $L_M \simeq 7.8$ . (c) Phase diagram of the model in the plane of interaction strength  $U$  and intensity of quasiperiodic hoppings  $V_2$ , adapted from Ref. [28].

$$d_i^\dagger = \sum_r \langle r|i \rangle c_r^\dagger, \quad d_i = \sum_r \langle i|r \rangle c_r, \quad (2)$$

where  $d_i^\dagger$  creates a particle in level  $i$ . In the following, we label  $d_i^\dagger = o_i^\dagger$ ,  $d_i^\dagger = p_i^\dagger$ , and  $d_i^\dagger = e_i^\dagger$  for  $i \in \text{OC}$ ,  $\text{FB}$ ,  $\text{E}$  respectively. Plugging Eq. 2 in Eq. 1 leads to the first-order (linear in  $U$ ) projected Hamiltonian:

$$H_{BP}^{(1)} = H_0 + H_{\text{FB-OC}} + H_{\text{FB-FB}} = \sum_{i \in hf} \varepsilon_i p_i^\dagger p_i + 4 \sum_{\substack{i,n \in \text{FB} \\ j \in \text{OC}}} V_{ijjn}^A p_i^\dagger p_n + \sum_{\substack{i,j \in \text{FB} \\ m,n \in \text{FB}}} V_{ijkl}^A p_i^\dagger p_j^\dagger p_m p_n, \quad (3)$$

where  $\varepsilon_i$  are the single-particle eigenenergies obtained from  $H_0$ ,  $V_{ijmn}^A = U/4 [V_{ijmn} - V_{jimn} - V_{ijnm} + V_{jinm}]$  due to antisymmetrization.  $H_{\text{FB-OC}}$  is the one-body interacting term arising due to ‘‘potential scattering’’ from electrons in the occupied band and  $H_{\text{FB-FB}}$  is the two-body interacting term projected into the FB space. Second-order corrections to Eq. 3 are obtained by accounting for virtual interband excitations. The full second-order Hamiltonian can be written as

$$H_{BP}^{(2)} = P_0 H_0 P_0 + P_0 V P_0 + \frac{P_0 V \bar{P} V P_0}{E - H_0}, \quad (4)$$

where  $P_0$  is the projection operator onto the unperturbed subspace that is spanned by states with no holes in the occupied band and no electrons in the empty band, and  $\bar{P} = \mathbb{I} - P_0$ .

Fig. 2 shows the Feynman diagrams for the terms arising from second-order band projection, where black,

blue and red lines correspond FB, OC and E states, respectively. For simplicity, we use the notation  $ab;cd = V_{ijkl}^A a_i^\dagger b_j^\dagger c_k d_l$ , with implicit Einstein’s notation.

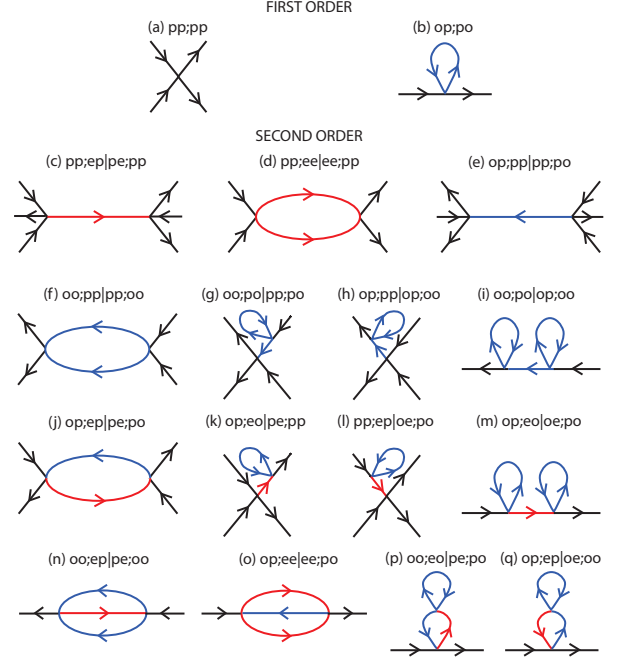


FIG. 2. Feynman diagrams for the effective Hamiltonian. FB, OC and E lines are depicted in black, blue and red, respectively. Time flows horizontally to the right.

We now re-write the full second-order effective Hamiltonian by combining all terms after normal ordering:

$$H_{BP}^{(2)} = \varepsilon_i p_i^\dagger p_i + V_{in}^{1b} p_i^\dagger p_n + V_{ijmn}^{2b} p_i^\dagger p_j^\dagger p_m p_n + V_{ijklmn}^{3b} p_i^\dagger p_j^\dagger p_k^\dagger p_l p_m p_n, \quad (5)$$

where  $V_{in}^{1b}$ ,  $V_{ijmn}^{2b}$  and  $V_{ijklmn}^{3b}$  are the one-body, two-body and three-body interacting terms in the FB space. A detailed derivation of Eq. 5 is given in Appendix A.

We now describe the different quantities that we used to characterize the ground-state phase diagram. To diagnose phase transitions and crossovers, we use the fidelity susceptibility, defined as [51]:

$$\chi_F = \lim_{\delta U \rightarrow 0} \left( -\frac{2 \ln F}{N \delta U^2} \right), \quad (6)$$

where  $F = |\langle \psi(U) | \psi(U + \delta U) \rangle|$  is the fidelity and  $\psi(U)$  is the many-body ground state for a given interaction strength  $U$ .

In order to distinguish between gapless and gapped phases, we study the charge gap:

$$\Delta_C = E(N_p + 1) + E(N_p - 1) - 2E(N_p), \quad (7)$$

where  $E(N_p)$  is the ground state energy for a system with  $N_p$  particles. At half-filling,  $N_p = N/2$ .

To explore the formation of charge order, we define the real-space density fluctuations as  $\langle \delta n_r \rangle = \langle n_r \rangle - 1/2$  and their corresponding Fourier transform  $\langle \delta n_k \rangle = 1/\sqrt{N} \sum_{r=0}^{N-1} e^{-i2\pi kr/N} \langle \delta n_r \rangle$ . Particle-hole symmetric [28] at half-filling imposes  $\langle \delta n_r \rangle = 0$ . Thus, in order to use  $\langle \delta n_k \rangle$  as a diagnostic tool, we add a symmetry breaking field to  $H_0$  in Eq. 1  $\varepsilon c_0^\dagger c_0$ , choosing  $\varepsilon = 2$ . In the gapless phase, the boundary fluctuations induced by the edge field are non-extensive and we have  $\langle \delta n_k \rangle \propto N^{-1/2}$  for any  $k$ . On the other hand, in the CDW phase  $\varepsilon$  selects a symmetry-broken CDW state with density fluctuations that scale as  $\langle \delta n_k \rangle \propto N^{1/2}$ , with all the wavevectors  $k$  connected to that state. A simple way to quantitatively distinguish these phases is through the inverse participation ratio (IPR) of the average of the density fluctuations in momentum space, defined as:

$$\text{IPR}_K(\langle \delta \mathbf{n} \rangle) = \frac{\sum_{k=0}^{N-1} |\langle \delta n_k \rangle|^4}{\left( \sum_{k=0}^{N-1} |\langle \delta n_k \rangle|^2 \right)^2}. \quad (8)$$

In the thermodynamic limit,  $N \rightarrow \infty$ ,  $\text{IPR}_K \sim N^{-1}$  for the LL phase, while  $\text{IPR}_K \sim N^0$  for the CDW phase [28].

Beyond the ground-state, we also explore low-lying excitations through the many-body density of states (DoS):

$$\rho(E) = \frac{1}{N} \sum_{\nu=1}^N \delta_\sigma(E - E_\nu)$$

where  $\nu$  labels excited many-body states and  $\delta_\sigma \simeq \exp(-\omega^2/2\sigma^2)/\sqrt{2\pi}\sigma$  is the Gaussian broadening of the delta-function with width  $\sigma$ , that we take to be of the order of the mean-level spacing.

With the aim of exploring the system's dynamical properties, we compute the regular component of the optical conductivity, within the framework of linear-response theory [52–58]:

$$\sigma_{reg}(\omega) = \frac{i}{\omega + i\eta} \left[ \frac{2}{N} \sum_{\nu \neq 0} \frac{|\langle \nu | J | 0 \rangle|^2}{\Delta E_0^\nu} + \frac{1}{N} \sum_{\nu \neq 0} \frac{|\langle \nu | J | 0 \rangle|^2}{\omega - \Delta E_0^\nu + i\eta} - \frac{1}{N} \sum_{\nu \neq 0} \frac{|\langle \nu | J | 0 \rangle|^2}{\omega + \Delta E_0^\nu + i\eta} \right], \quad (9)$$

where  $J = -i \sum_{r=0}^{N-1} t_r (c_r^\dagger c_{r+1} - c_{r+1}^\dagger c_r)$  is the current operator,  $\Delta E_0^\nu = E_\nu - E_0$  is the energy shift between the ground state and the excited state and  $\omega$  is the frequency of the vector field,  $A(\omega)$ , driving the system's response. This probing frequency is assumed to be smaller than the inter-band gap, in which case the intraband transitions can be computed within the BP formalism, as shown in Appendix , where the current term,  $\sum_{\nu \neq 0} |\langle \nu | J | 0 \rangle|^2$ , yields:

$$\sum_{\nu \neq 0} |\langle \nu | J | 0 \rangle|^2 = \sum_{\nu \neq 0} \langle 0 | \sum_{j,k \in \text{FB}} -i \sum_{r=0}^{N-1} t_r [\langle j | r \rangle \langle r+1 | k \rangle - \langle j | r+1 \rangle \langle r | k \rangle] p_j^\dagger p_k | \nu \rangle \times \langle \nu | i \sum_{l,m \in \text{FB}} t_r [\langle l | r+1 \rangle \langle r | m \rangle - \langle l | r \rangle \langle r+1 | m \rangle] p_l^\dagger p_m | 0 \rangle. \quad (10)$$

Further details on the derivation of Eq. 9, computation of its real part and BP implementation are presented in Appendix C.

The properties of the system's dynamical response are also explored using the spectral weight of the regular part of the optical conductivity in the  $\omega \ll \Delta$  regime:

$$K(\Omega) = \sum_{\omega < \Omega} \frac{2}{\pi} \Re [\sigma_{reg}(\omega)] \delta\omega, \quad (11)$$

where  $\Omega$  covers the energy spectrum of the excited states in the FB.

Finally, for reference, we provide the system sizes and rational approximants used for all the calculations in Ta-

$N$	30	44	62	76	94	108
$\tau$	17/30	25/44	35/62	43/76	53/94	61/108

TABLE I. Sizes and rational approximants used for numerical computations.

ble I.

### III. RESULTS AND DISCUSSION

We begin by benchmarking the BP approach against the numerically exact results previously obtained using

DMRG in Ref. [28]. Our first key finding is that a projection restricted to first order in the interaction strength fails to reproduce any of the phase transitions of the full model. This result is non-trivial and, at first sight, surprising: first-order band projection is routinely employed in the context of fractional quantum Hall systems and other interacting models with well-separated bands, where it typically captures the correct qualitative structure of the correlated phases [41, 59–62].

A closer analysis reveals that, in the present quasiperiodic narrow-band system, this expectation breaks down. As shown explicitly in Appendix D, a specific second-order virtual process involving remote bands provides a qualitatively essential contribution, without which the effective Hamiltonian fails to capture the interaction-driven instabilities observed in the full DMRG treatment.

In the following, all results are therefore obtained using the second-order effective Hamiltonian, Eq. (5), which incorporates these virtual interband excitations in a controlled manner.

### A. Ground-state phase diagram

We first consider the case where interactions are introduced in the extended single-particle regime, focusing on  $V_2 = 0.9$ . Figure 3(a) shows the fidelity susceptibility  $\chi_F$  as a function of interaction strength  $U$  for several system sizes. A pronounced peak develops at a critical interaction  $U = U_c$ , with a height that grows with system size, signaling a quantum phase transition.

The nature of the phases on either side of this transition is clarified by examining the charge gap  $\Delta_C$  (Fig. 3(b)), and the momentum-space inverse participation ratio of the density fluctuations,  $\text{IPR}_K(\langle\delta n\rangle)$  [Fig. 3(c)]. For  $U < U_c$ , both quantities decrease with increasing system size, consistent with a gapless and uncorrelated phase, which we identify as a LL. In contrast, for  $U > U_c$  both  $\Delta_C$  and  $\text{IPR}_K(\langle\delta n\rangle)$  approach finite values in the thermodynamic limit, indicating the onset of a gapped CDW phase with long-range order.

At finite quasiperiodic modulation, the LL–CDW transition is expected to be of the Berezinskii–Kosterlitz–Thouless (BKT) type, as in the periodic case. However, the structure of the ordered phase differs markedly from that at  $V_2 = 0$ . In the absence of quasiperiodicity, the CDW is characterized by a single ordering wavevector  $k = \pi$  [63], whereas for  $V_2 \lesssim 1$  the charge order contains contributions from multiple wavevectors inherited from the quasiperiodic modulation, in agreement with earlier DMRG results [28].

We now turn to the strongly quasiperiodic regime,  $V_2 \geq 2$ , where the non-interacting system hosts critical single-particle states. Figure 4(a) shows the fidelity susceptibility as a function of  $U$ . In contrast to the sharp LL–CDW transition observed at  $V_2 = 0.9$ , here

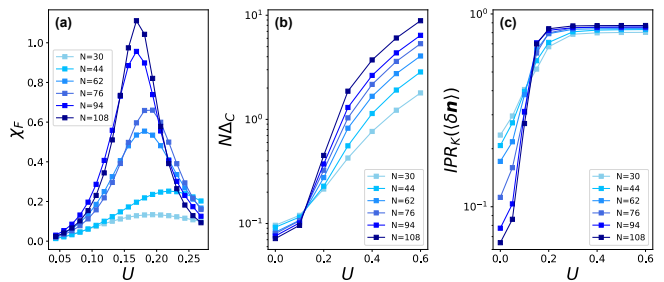


FIG. 3. LL-CDW phase transition determined by the finite-size scaling analysis of: (a) the fidelity susceptibility ( $\chi_F$ ), defined by Eq. 6 with  $\delta U = 1.25 \times 10^{-2}$ ; (b) the charge gap ( $\Delta_C$ ), defined by Eq. 7; (c) the IPR of the average of the density fluctuations in momentum space ( $\text{IPR}_K(\langle\delta n\rangle)$ ), defined by Eq. 8. Results are averaged over 10 random configurations of  $\phi$  and  $\theta$ .

$\chi_F$  displays a broad peak around  $U \simeq 0.25$ . As shown in Ref. [28], this feature corresponds to a crossover between a quasifractal charge-density-wave (qf-CDW) regime at weak interactions and a more conventional CDW phase at larger  $U$ . Although finite-size effects prevent a clear saturation of  $\chi_F$  in the present system sizes, the markedly smoother behavior of the peak already distinguishes this crossover from a true phase transition.

Together, these results demonstrate that second-order band projection accurately reproduces the full ground-state phase diagram of the model, including both the LL–CDW transition in the extended regime and the qf-CDW–CDW crossover in the critical regime.

### B. Low-energy excitation spectrum

Having established the validity of the BP approach at the level of ground-state properties, we now turn to low-energy excitations, which were not accessible in the original DMRG study. Excited states are obtained by exact diagonalization within the projected narrow-band Hilbert space.

Figure 4(c) shows the many-body density of states (DoS) for representative points in the phase diagram, indicated schematically in Fig. 4(b). In the LL phase ( $V_2 = 0.9$ ,  $U = 0.075$ ), the DoS extends continuously to zero energy, reflecting the presence of gapless neutral excitations. Upon entering the CDW phase ( $V_2 = 0.9$ ,  $U = 0.25$ ), a clear excitation gap opens between the twofold degenerate ground-states and the excited state band, consistent with the breaking of translational symmetry and the formation of long-range charge order.

In the strongly quasiperiodic regime, the qf-CDW phase ( $V_2 = 2$ ,  $U = 0.1$ ) exhibits qualitatively different behavior. While the system remains ordered, the neutral gap becomes strongly suppressed and the twofold ground-state degeneracy associated with CDW order is weakly

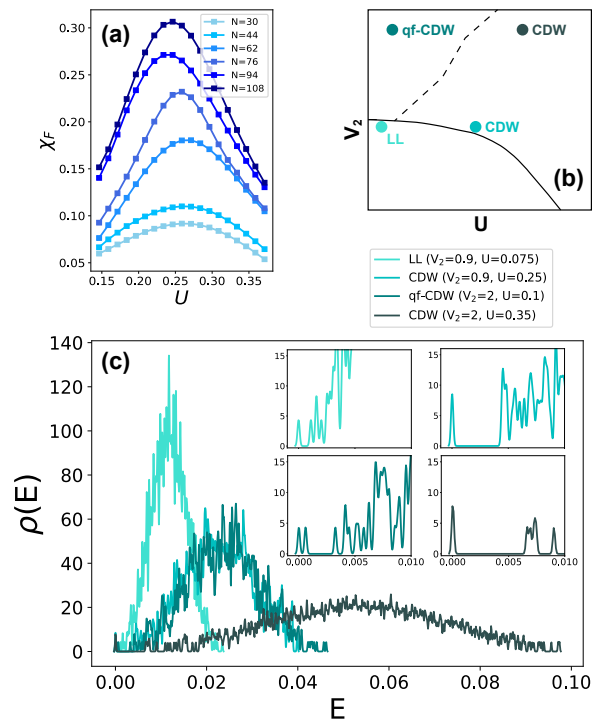


FIG. 4. (a) Fidelity susceptibility ( $\chi_F$ ) for  $V_2 = 2$ . (b) Schematic phase diagram indicating the phase space points that are used for computing the density of states and the optical conductivity in panel (c). (c) Density of states computed with a Gaussian width of  $\sigma = 10^{-4}$  and  $N = 94$  for the following phase-space points:  $V_2 = 0.9, U = 0.075$  (LL);  $V_2 = 0.9, U = 0.25$  (CDW);  $V_2 = 2, U = 0.1$  (qf-CDW);  $V_2 = 2, U = 0.275$  (CDW). Inset shows a close-up at low energies.

lifted. This is consistent with the picture of a quasifractal ordered state, where charge modulations involve a large — though finite — number of incommensurate wavevectors and finite-size effects are particularly pronounced. At larger interaction strength ( $V_2 = 2, U = 0.275$ ), the system crosses over into a conventional CDW phase, and a robust neutral gap is recovered.

### C. Optical conductivity

We now examine the dynamical response of the system through the regular part of the optical conductivity,  $\sigma_{\text{reg}}(\omega)$ , focusing on frequencies well below the interband gap where intraband processes dominate. Figure 5(a) shows  $\text{Re}[\sigma_{\text{reg}}(\omega)]$  for  $V_2 = 0.9$ .

In the non-interacting ( $U = 0$ ) extended phase, the regular part of the conductivity is strongly suppressed at low frequencies. In this regime, the quasiperiodic system is well approximated by a commensurate superlattice with a large unit cell, and the narrow band near  $E = 0$  behaves effectively as a Bloch band. Consequently, intra-

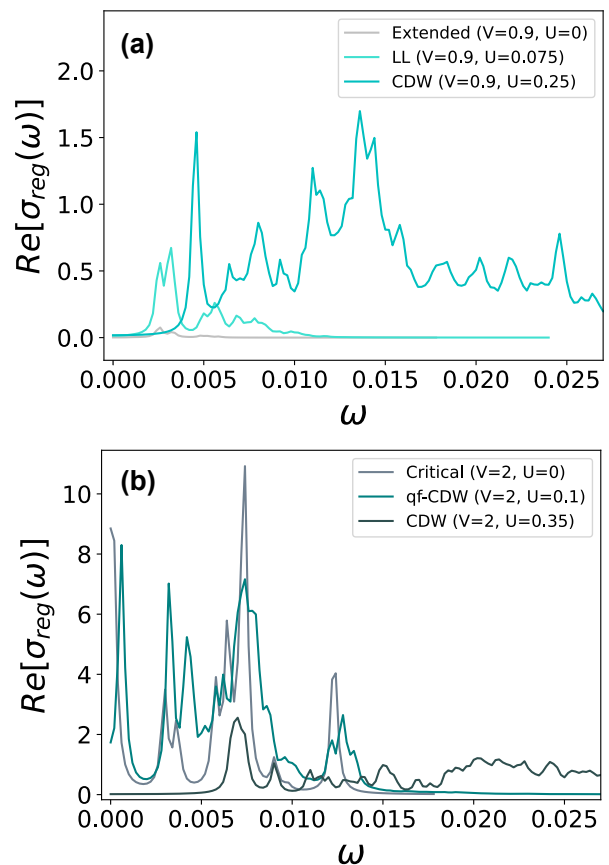


FIG. 5. Real component of the regular part of the optical conductivity,  $\Re[\sigma_{\text{reg}}(\omega)]$ , Eq. 9, computed for  $N = 94$ , with  $\delta\omega = 2 \times 10^{-4}$ , Lorentzian width of  $\eta = 2 \times 10^{-4}$  and random shift and twist, for: (a) extended states ( $V_2 = 0.9, U = 0$ ), LL ( $V_2 = 0.9, U = 0.075$ ) and CDW ( $V_2 = 0.9, U = 0.25$ ); (b) critical states ( $V_2 = 2, U = 0$ ), qf-CDW ( $V_2 = 2, U = 0.1$ ) and CDW ( $V_2 = 2, U = 0.35$ ).

band contributions are entirely captured by the Drude peak at  $\omega = 0$ , while  $\sigma_{\text{reg}}(\omega)$  contains only interband processes and vanishes at small  $\omega$  (see Appendix IV).

As  $V_2$  increases toward and beyond unity, spectral gaps open increasingly close to the Fermi energy, enabling low-energy intraband transitions. For  $V_2 \geq 1$ , the Drude weight vanishes in the thermodynamic limit and the spectral weight is transferred to the regular part of the conductivity, resulting in a pronounced low-frequency response even in the non-interacting critical phase [Fig. 5(b)].

Turning on interactions at  $V_2 = 0.9 < 1$  enhances the low-frequency optical response in the LL phase, as expected from Luttinger-liquid theory, where  $\sigma(\omega) \sim \omega^3$  at small  $\omega$  [64]. In contrast, CDW phase ( $U = 0.25$ ) phase exhibits a well-defined optical gap [58, 65, 66] [see Fig. 5(a)], reflecting the finite energy required to excite particle-hole pairs across the charge gap.

In the strongly quasiperiodic regime ( $V_2 \gtrsim 2$ ), the non-interacting critical phase already displays a strong opti-

cal response at low frequencies. Upon introducing weak interactions ( $U = 0.1$ ), the system enters the qf-CDW regime, which remains characterized by an almost vanishing optical gap and a substantial low-frequency conductivity. Increasing  $U$  further drives the system into the CDW phase, where a clear optical gap re-emerges, mirroring the behavior observed at  $V_2 = 0.9$ .

Phase	$K(\Omega)$
Extended ( $V = 0.9, U = 0$ )	$6 \times 10^{-5}$
LL ( $V = 0.9, U = 0.075$ )	$9 \times 10^{-4}$
CDW ( $V = 0.9, U = 0.25$ )	$1.1 \times 10^{-2}$
Critical ( $V = 2, U = 0$ )	$1.6 \times 10^{-2}$
qf-CDW ( $V = 2, U = 0.1$ )	$2.3 \times 10^{-2}$
CDW ( $V = 2, U = 0.35$ )	$2.1 \times 10^{-2}$

TABLE II. Spectral weight of the regular part of the optical conductivity for the intraband transitions in the flatband.

Additional insight is obtained by considering the integrated spectral weight of the regular part of the conductivity,  $K(\Omega)$ , defined in Eq. 11. The values of  $K(\Omega)$  for different phases are summarized in Table II.

In the extended non-interacting phase,  $K(\Omega)$  is extremely small, reflecting the fact that nearly all spectral weight resides in the Drude peak. By contrast, both CDW and qf-CDW phases exhibit significantly larger values of  $K(\Omega)$ , of order  $10^{-2}$ , indicating that the dominant contribution to the optical response arises from finite-frequency processes. The LL phase occupies an intermediate regime, with a spectral weight larger than in the extended phase but still substantially smaller than in the ordered phases.

Overall, these results show that the redistribution of spectral weight between the Drude peak and the regular part of the optical conductivity provides a clear dynamical fingerprint of the different phases induced by the interplay of quasiperiodicity and interactions.

#### IV. CONCLUSIONS

In this work, we have demonstrated that band projection can provide an accurate and efficient description of interacting quasiperiodic systems, provided that virtual processes involving remote bands are properly taken into account. Using a one-dimensional narrow-band quasiperiodic model as a test bed, we showed that a projection restricted to first order in the interaction strength fails to reproduce the correct ground-state phase diagram. This breakdown contrasts with the widespread success of first-order band projection in translationally invariant flatband systems and highlights a fundamental difference introduced by quasiperiodicity.

By incorporating second-order virtual interband processes, we obtained an effective Hamiltonian that quan-

titatively reproduces all phases previously identified using numerically exact DMRG calculations. In particular, the second-order band-projected theory captures the interaction-driven transition between the Luttinger liquid and charge-density-wave phases in the extended regime, as well as the crossover between the quasifractal charge-density-wave regime and the conventional CDW phase in the strongly quasiperiodic regime. Our results identify a specific class of second-order processes as being qualitatively essential for stabilizing correlated phases in narrow-band quasiperiodic systems.

Beyond ground-state properties, the controlled band projection scheme allowed us to investigate low-energy neutral excitations and dynamical response functions that are difficult to access with DMRG. We showed that the Luttinger liquid phase is characterized by gapless neutral and optical excitations, while the CDW phase exhibits finite neutral and optical gaps. In contrast, the quasifractal CDW regime displays strongly suppressed—though finite—neutral, charge, and optical gaps, together with a redistribution of optical spectral weight toward low frequencies. These features provide clear dynamical signatures distinguishing the different interaction-driven regimes.

Our findings establish band projection, when extended beyond first order, as a reliable tool for studying correlated quasiperiodic systems. More broadly, they suggest a viable and controlled route to explore interacting narrow-band quasiperiodic systems in higher dimensions, where exact numerical methods are severely limited. This is particularly relevant for moiré materials, such as twisted bilayer or trilayer [67, 68] graphene and twisted bilayer graphene on hBN [69], where quasiperiodicity and narrow-bands naturally coexist and where the role of interactions in the absence of strict translational symmetry remains an open and timely problem.

#### ACKNOWLEDGMENTS

The authors MG and PR acknowledge partial support from Fundação para a Ciência e Tecnologia (FCT-Portugal) through Grant No. UID/CTM/04540/2019. FR, MG and PR acknowledge support by FCT through Grant No. UIDB/04540/2020. BA and EVC acknowledge partial support from FCT-Portugal through Grant No. UIDB/04650/2020. MG acknowledges further support from FCT-Portugal through the Grant SFRH/BD/145152/2019. BA acknowledges further support from FCT-Portugal through Grant No. CEECIND/02936/2017/CP1458/CT0010. We finally acknowledge the Tianhe-2JK cluster at the Beijing Computational Science Research Center (CSRC) and the OBLIVION supercomputer, through projects 2022.15910.CPCA.A1 and 2023.14361.CPCA.A1 (based

at the High Performance Computing Center - University of Évora) funded by the ENGAGE SKA Research Infrastructure (reference POCI-01-0145-FEDER-022217 - COMPETE 2020 and the Foundation for Science and Technology, Portugal) and by the BigData@UE project (reference ALT20-03-0246-FEDER-000033 - FEDER and the Alentejo 2020 Regional Operational Program. Computer assistance was provided by CSRC's and OBLIVION's support teams.

## APPENDIX A: BAND PROJECTION TECHNIQUE IN QUASIPERIODIC SYSTEMS

The band projection technique is an effective framework for studying many-body systems characterized by a flatband. This approach enables computational analysis of significantly larger system sizes than would be feasible using conventional exact diagonalization applied to the full system.

Here we describe the detailed implementation of this technique, taking the example considered in this work of a narrow-band quasi-periodic system with the Hamiltonian given in Eq. 1. At  $V_2 = 1$ , a narrow-band (FB) is energetically separated from the remote bands. For interactions that are weak when compared to the band gap ( $\Delta$ ) but strong when compared to the bandwidth ( $W$ ),  $W \ll U \ll \Delta$ , interaction-induced mixing between the FB and the lower (or upper) bands is weak. In this regime, it is therefore well justified to account for the mixing between the narrow-band subspace and the remote bands perturbatively [41, 59].

Working in the band basis introduced in Eq. 2, the single-particle Hamiltonian is diagonal and given by  $H_0 = \sum_i \varepsilon_i d_i^\dagger d_i$ , where  $\varepsilon_i$  are the single-particle eigenenergies:

$$\begin{aligned} H_0 &= - \sum_r t_r \left( c_r^\dagger c_{r+1} + c_{r+1}^\dagger c_r \right) \\ H_0 &= - \sum_i \sum_r t_r \left( \langle i|r \rangle \langle r+1|i \rangle + \langle i|r+1 \rangle \langle r|i \rangle \right) d_i^\dagger d_i \\ H_0 &= \sum_i \varepsilon_i d_i^\dagger d_i. \end{aligned} \quad (\text{A1})$$

Since we work at half-filling of the narrow-band and consider weak interactions when compared with the bandgap, we can assume that the states on the remote bands are “frozen”. In particular, we assume that the eigenstates in the lower-energy and higher-energy remote bands are respectively occupied and empty, only renormalizing the narrow-band through virtual processes.

The interacting part of the Hamiltonian in Eq. 1 can be written as:

$$\begin{aligned} V &= U \sum_r \left[ \sum_{\substack{i,j, \\ m,n}} \langle i|r \rangle d_i^\dagger \langle j|r+1 \rangle d_j^\dagger \langle r+1|m \rangle d_m \langle r|n \rangle d_n \right] \\ &= U \sum_r \left[ \sum_{\substack{i,j, \\ m,n}} \langle i|r \rangle \langle j|r+1 \rangle \langle r+1|m \rangle \langle r|n \rangle d_i^\dagger d_j^\dagger d_m d_n \right] \\ &= \sum_{\substack{i,j, \\ m,n}} V_{ijmn}^A d_i^\dagger d_j^\dagger d_m d_n, \end{aligned} \quad (\text{A2})$$

where  $V_{ijmn}^A = U/4 [V_{ijmn} - V_{jimn} - V_{ijnm} + V_{jinm}]$  are

the antisymmetrized interaction matrix elements  $V_{ijmn} = \sum_r \langle i|r \rangle \langle j|r+1 \rangle \langle r+1|m \rangle \langle r|n \rangle$ .

By taking the OC and E eigenstates as fully occupied and empty, i.e.,  $d_i^\dagger d_j \rightarrow \langle d_i^\dagger d_j \rangle = \delta_{ij}$ ,  $i, j \in \text{OC}$  and  $d_i^\dagger d_j \rightarrow \langle d_i^\dagger d_j \rangle = 0$ ,  $i, j \in \text{E}$ , the projected Hamiltonian to first order in interaction strength is given by

$$H_{BP}^{(1)} = H_0 + H_{FB-OC} + H_{FB-FB} = \sum_{i \in hf} \varepsilon_i d_i^\dagger d_i + 4 \sum_{\substack{i,l \in FB \\ j \in OC}} V_{ijjn}^A d_i^\dagger d_j + \sum_{\substack{i,j \in FB \\ m,n \in FB}} V_{ijmn}^A d_i^\dagger d_j^\dagger d_m d_n, \quad (\text{A3})$$

where  $H_{FB-OC}$  destroys and creates one particle in the OC band and another particle in the FB, and  $H_{FB-FB}$  is the projected interaction in the FB subspace.

If the first-order approximation in Eq. C6 fails to capture the expected behavior in the  $U \ll \Delta$  regime, which is the case in our model, second-order perturbation corrections must be included. To proceed with the derivation, we adopt a more straightforward notation. Operators will be written as  $o^\dagger, o; p^\dagger, p; e^\dagger, e$ ; referring to the OC band (o); partially filled band/FB (p); and E band (e). Operator indices will be denoted with a bottom bar, no bar and top bar, to indicate they belong to the occupied band, partially filled band and empty band, respectively. We also use Einstein's notation in what follows. Eq. A3 can therefore be more compactly written as:

$$H_{BP}^{(1)} = H_0 + H_{FB-OC} + H_{FB-FB} = \varepsilon_i p_i^\dagger p_i + 4V_{ioon}^A p_i^\dagger p_n + V_{ijmn}^A p_i^\dagger p_j^\dagger p_m p_n. \quad (\text{A4})$$

which implies that we can write the effective Hamiltonian up to second-order in interaction strength as:

$$H_{BP}^{(2)} = P_0 H_0 P_0 + P_0 V P_0 + \frac{P_0 V \bar{P} V P_0}{E - H_0}, \quad (\text{A8})$$

where we used the fact that  $\frac{1}{P(E-H_0)\bar{P}}$  is diagonal in the occupation number basis.

The non-zero contributions in first and second-order

To introduce BP up to second order, we first rewrite  $H_{BP}^{(1)}$  as:

$$H_{BP}^{(1)} = P_0 H_0 P_0 + P_0 V P_0 \quad (\text{A5})$$

where  $H_0$  and  $V$  are defined in Eq. C1 and  $P_0$  is the projection operator into the narrow-band eigenstates,  $P_0 = |\psi_0\rangle\langle\psi_0|$ , where:

$$|\psi_0\rangle = |\text{OC}\rangle|\text{FB}\rangle = \prod_{\alpha} o_{\alpha}^{\dagger} \prod_{\beta} p_{\beta}^{\dagger} |0\rangle.$$

Recall that the OC and E bands do not influence the dimensionality of  $H_{BP}$ , since the states are either completely full (OC) or completely empty (E):  $|111 \dots 111\rangle|\text{FB}\rangle|000 \dots 000\rangle$ .

Introducing  $\bar{P} = \mathbb{I} - P_0$ , the full Hamiltonian can be written exactly as

$$\mathbf{H} = \begin{pmatrix} P_0 H P_0 & P_0 H \bar{P} \\ \bar{P} H P_0 & \bar{P} H \bar{P} \end{pmatrix} = \begin{pmatrix} P_0 H P_0 & P_0 V \bar{P} \\ \bar{P} V P_0 & \bar{P} H \bar{P} \end{pmatrix}, \quad (\text{A6})$$

where we used  $P_0 H_0 \bar{P} = 0$ , since  $H_0$  is diagonal.

Now we consider the Green function  $\mathcal{G} = (E - \mathbf{H})^{-1}$  and define our effective projected Hamiltonian as  $P_0 \mathcal{G} P_0 = (E - \mathbf{H}_{BP})^{-1}$ . Explicitly, we have:

$$\begin{aligned} \mathcal{G} &= (E - \mathbf{H})^{-1} = \begin{pmatrix} P_0(E - H)P_0 & -P_0 V \bar{P} \\ -\bar{P} V P_0 & \bar{P}(E - H)\bar{P} \end{pmatrix}^{-1} \\ &= \begin{pmatrix} \left( E - P_0 H P_0 - P_0 V \bar{P} \frac{1}{\bar{P}(E-H)\bar{P}} \bar{P} V P_0 \right)^{-1} & \dots \\ \dots & \dots \end{pmatrix}, \end{aligned} \quad (\text{A7})$$

perturbation theory can be represented using Feynman diagrams. These diagrams represent the interactions between the flat, occupied, and empty bands, and their combinatorial contributions are detailed in Fig. 2. For simplicity, we use a shorthand notation, e.g.,  $ee; pp$ , to represent  $V_{ijkl}^A e_i^\dagger e_j^\dagger p_k p_l$ .

We now analyse the contributions to  $P_0 V \bar{P} V P_0$  separately.

### Terms with flatband and empty band operators

These terms can involve the excitation of one electron, Fig. 2 (c), or two electrons, Fig. 2 (d), from FB to E. For such contributions,  $P_0 V \bar{P} V P_0$  can be written as:

$$\langle \psi_0 | \begin{pmatrix} 2pp; ep \\ pp; ee \end{pmatrix} | \psi_I \rangle \frac{1}{E - H_0} \langle \psi_I | \begin{pmatrix} 2pe; pp \\ ee; pp \end{pmatrix} | \psi_0 \rangle, \quad (\text{A9})$$

where the factor 2 stems from considering all contributions, e.g.:

$$\begin{aligned} p_i p_j; e_{\bar{k}} p_l + p_i p_j; p_k e_{\bar{l}} &= p_i p_j; e_{\bar{k}} p_l - p_i p_j; e_{\bar{l}} p_k \\ &= p_i p_j; e_{\bar{k}} p_l + p_i p_j; e_{\bar{k}} p_l \\ &= 2p_i p_j; e_{\bar{k}} p_l. \end{aligned} \quad (\text{A10})$$

Note that terms that do not conserve particle number such as  $(2pp; ep|epp)$  are not allowed.

From Eq. A9 we obtain the following terms in second order:

$$\begin{aligned} 4(pp; ep|pe; pp) & \text{ 3-body} \\ (pp; ee|ee; pp) & \text{ 2-body} \end{aligned}$$

To exemplify how such terms are explicitly evaluated, we take  $pp; ep|pe; pp$ , which yields

$$\begin{aligned} 4(pp; ep|pe; pp) &= 4V_{ijkl}^A V_{m\bar{n}rs}^A p_i^\dagger p_j^\dagger e_{\bar{k}} p_l \frac{1}{(-\Delta E_{rs}^{\bar{k}m})} p_m^\dagger e_{\bar{n}}^\dagger p_r p_s = 4V_{ijkl}^A V_{m\bar{n}rs}^A p_i^\dagger p_j^\dagger p_l \frac{1}{(-\Delta E_{rs}^{\bar{k}m})} p_m^\dagger p_r p_s e_{\bar{k}} e_{\bar{n}}^\dagger \\ &= 4V_{ijkl}^A V_{m\bar{n}rs}^A p_i^\dagger p_j^\dagger p_l \frac{1}{(-\Delta E_{rs}^{\bar{k}m})} p_m^\dagger p_r p_s \delta_{\bar{k}n} = \frac{4}{\Delta E_{rs}^{\bar{k}m}} V_{ijkl}^A V_{m\bar{k}rs}^A p_i^\dagger p_j^\dagger p_l p_m^\dagger p_r p_s \\ &= \frac{4}{\Delta E_0^{\bar{k}}} V_{ijkl}^A V_{m\bar{k}rs}^A \left[ -p_i^\dagger p_j^\dagger p_m^\dagger p_l p_r p_s + p_i^\dagger p_j^\dagger p_r p_s \delta_{lm} \right] \\ &= \frac{4}{\Delta E_0^{\bar{s}}} V_{ij\bar{s}l}^A V_{k\bar{s}mn}^A \left[ -p_i^\dagger p_j^\dagger p_k^\dagger p_l p_m p_n + p_i^\dagger p_j^\dagger p_m p_n \delta_{kl} \right] \\ &= \frac{4}{\Delta E_0^{\bar{s}}} \left[ -V_{ij\bar{s}l}^A V_{k\bar{s}mn}^A p_i^\dagger p_j^\dagger p_k^\dagger p_l p_m p_n + V_{ij\bar{s}k}^A V_{k\bar{s}mn}^A p_i^\dagger p_j^\dagger p_m p_n \right], \end{aligned} \quad (\text{A11})$$

where  $\Delta E_{rs}^{\bar{k}m}$  corresponds to the single-particle energy needed to destroy two particles at indices  $r, s$  and create them at indices  $\bar{k}, m$ . Since, in our model, all states on the FB have energy close to the Fermi Energy, we consider  $\Delta E_0^{\bar{s}} = -\epsilon_s$ , the difference between  $E_F = 0$  and the state created at  $\bar{s}$ .

### Terms with flatband and occupied band operators

These terms correspond to the diagrams (e)-(i) in Fig.2. For such contributions,  $P_0 V \bar{P} V P_0$  can be written as:

$$\langle \psi_0 | \begin{pmatrix} 2op; pp \\ oo; pp \\ 2oo; po \\ 2op; pp \\ 2oo; po \end{pmatrix} | \psi_I \rangle \frac{1}{E - H_0} \langle \psi_I | \begin{pmatrix} 2pp; po \\ pp; oo \\ 2pp; po \\ 2op; oo \\ 2op; oo \end{pmatrix} | \psi_0 \rangle, \quad (\text{A12})$$

where, once again, we ignore zero contributions, as well as contributions that do not conserve particle number. From Eq. A12 we obtain the following non-vanishing terms in second-order:

$$\begin{aligned} 4(op; pp|pp; po) & \text{ 3-body} \\ (oo; pp|pp; oo) & \text{ 2-body} \\ 4(oo; po|pp; po) & \text{ 2-body} \\ 4(op; pp|op; oo) & \text{ 2-body} \\ 4(oo; po|op; oo) & \text{ 1-body} \end{aligned}$$

### Terms with operators in all bands

These terms are depicted by the diagrams (j)-(q) in Fig.2.  $P_0 V \bar{P} V P_0$  can be written as:

$$\langle \psi_0 | \begin{pmatrix} 4op; ep \\ 4op; eo \\ 2pp; ep \\ 4op; eo \\ 2oo; ep \\ 2op; ee \\ 2oo; eo \\ 4op; ep \end{pmatrix} |\psi_I\rangle \frac{1}{E_0 - \bar{H}_0} \langle \psi_I | \begin{pmatrix} 4pe; po \\ 2pe; pp \\ 4oe; po \\ 4oe; po \\ 2pe; oo \\ 2ee; po \\ 4pe; po \\ 2oe; oo \end{pmatrix} |\psi_0\rangle, \tag{A13}$$

16(*op; ep; pepo*) 2 – body

8(*op; eo|pe; pp*) 2 – body

8(*pp; ep|oe; po*) 2 – body

16(*op; eo|oe; po*) 1 – body

4(*oo; ep|pe; oo*) 1 – body

4(*op; ee|ee; po*) 1 – body

8(*oo; eo|pe; po*) 1 – body

8(*op; ep|oe; oo*) 1 – body

**Full effective Hamiltonian**

From Eq. A13 we obtain the following terms in second-order:

The full second-order effective Hamiltonian is obtained by combining all terms, after normal ordering:

$$H_{BP}^{(2)} = \varepsilon_i p_i^\dagger p_i + V_{in}^{1b} p_i^\dagger p_n + V_{ijmn}^{2b} p_i^\dagger p_j^\dagger p_m p_n + V_{ijklmn}^{3b} p_i^\dagger p_j^\dagger p_k^\dagger p_l p_m p_n, \tag{A14}$$

where we have explicitly:

$$\begin{aligned}
V_{in}^{1b} &= 4V_{irrn} + \sum_{\text{second-order terms}} \\
&= 4V_{irrn} + \frac{8}{\Delta E_r^0} V_{rikl} V_{lknr} + \frac{8}{\Delta E_{rs}^{00}} V_{rsnl} V_{ilsr} + \frac{32}{\Delta E_r^0} V_{srks} V_{kinr} + \frac{16}{\Delta E_r^0} V_{srns} V_{mimr} \\
&+ \frac{16}{\Delta E_0^s} V_{risl} V_{l\bar{s}nr} - \frac{16}{\Delta E_0^s} V_{ri\bar{s}r} V_{j\bar{s}mn} + \frac{16}{\Delta E_0^s} V_{ri\bar{s}r} V_{m\bar{s}nm} + \frac{8}{\Delta E_{rs}^{0k}} V_{r\bar{s}kn} V_{i\bar{k}rs} \\
&+ \frac{8}{\Delta E_{k0}^{\bar{r}s}} V_{ki\bar{r}s} V_{\bar{s}rnk} + \frac{32}{\Delta E_r^k} V_{r\bar{s}ks} V_{i\bar{k}nr}. \tag{A15}
\end{aligned}$$

$$\begin{aligned}
V_{ijmn}^{2b} &= V_{ijmn} + \sum_{\text{second-order terms}} \\
&= V_{ijmn} + \frac{4}{\Delta E_0^s} V_{ij\bar{s}k} V_{k\bar{s}mn} + \frac{2}{\Delta E_{00}^{\bar{r}s}} V_{ij\bar{r}s} V_{\bar{s}rmn} + \frac{16}{\Delta E_r^0} V_{riml} V_{jlnr} + \frac{2}{\Delta E_{rs}^{00}} V_{rsmn} V_{ij\bar{s}r} \\
&+ \frac{16}{\Delta E_r^0} V_{srms} V_{ijnr} - \frac{16}{\Delta E_r^s} V_{ri\bar{s}m} V_{j\bar{s}nr} - \frac{16}{\Delta E_0^s} V_{ri\bar{s}r} V_{j\bar{s}mn}. \tag{A16}
\end{aligned}$$

$$V_{ijklmn}^{3b} = \sum_{\text{second-order terms}} = -\frac{4}{\Delta E_0^s} V_{ij\bar{s}l} V_{k\bar{s}mn} + \frac{4}{\Delta E_r^0} V_{rilm} V_{jknr}. \tag{A17}$$

## APPENDIX B: BENCHMARK OF THE OPTICAL CONDUCTIVITY

In the implementation of the band projected optical conductivity, given by Eq. 10, we restricted our analysis to operators within the FB (see Eq. C31). For many-body systems up to second-order in perturbation theory, including operators from the other bands, *e.g.*, destroying a state in the occupied (OC) band and creating one in the FB, would demand performing exact diagonalization (ED) for every state annihilated in the OC band, which is computationally unfeasible for larger system sizes.

Here we show that, in the far-infrared regime ( $\omega \ll 1$ ) at half-filling, the optical conductivity can be accurately

captured by limiting the operators to the FB. Figure B1 presents the benchmarking of the optical conductivity in the single-particle picture, computed with the operators restricted to the FB (red curves) and with the operators acting also in the remote bands (blue squares). The results are shown for extended ( $V_2 = 0.9$ , [a] – [c]) and critical states ( $V_2 = 1.1$ , [d] – [f]), for selected system sizes ( $N = 94, 484, 998$ ). The value of the Drude weight is indicated in each of these panels.

As can be seen more clearly in panel [g], while the Drude weight has a finite value for extended states ( $D \sim N^0$ ), it goes to zero in the thermodynamic limit for critical states ( $D \sim N^{-1}$ ). Since for extended states the spectral weight is mainly concentrated in the Drude peak, the regular component of the optical conductivity displays reduced values, as expected.

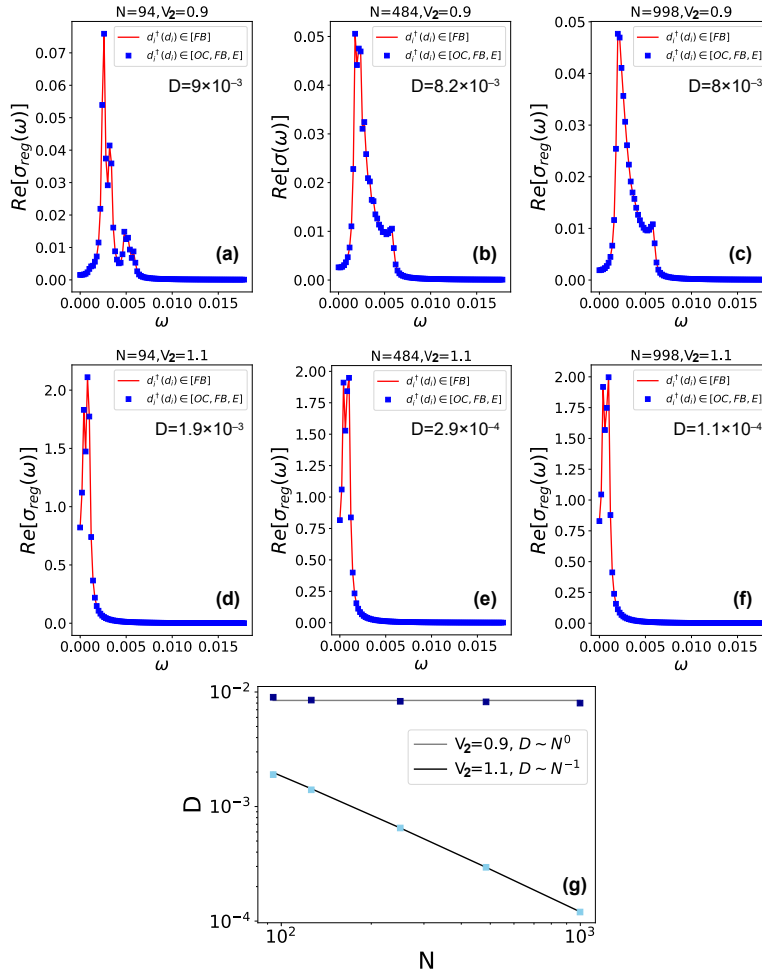


FIG. B1. Real component of the finite-frequency optical conductivity in the far infrared regime, computed with operators restricted to the FB (red curves) and operators applied to all bands (blue squares). Interaction strength is set to zero to make the computation with the full operators feasible. Results for extended (critical) states are shown in [a] – [c] ([d] – [f]), with  $\eta = 2 \times 10^{-4}$ . Panel [g] shows the scaling of the Drude weight for extended ( $D \sim N^0$ ) and critical ( $D \sim N^{-1}$ ) states.

Figure B2 presents the optical conductivity for  $N = [1000, 5000, 10000, 13000]$  and  $V_2 = [0.9, 1.1]$ . The results for the different system sizes are qualitative similar and converge as  $N$  gets closer to the thermodynamic limit, both for extended states and critical states.

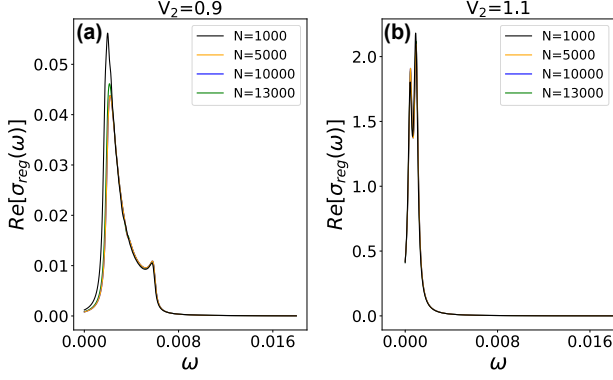


FIG. B2. Real component of the finite-frequency optical conductivity in the far infrared regime, for  $N = [1000, 5000, 10000, 13000]$ , with  $\eta = 2 \times 10^{-4}$ . The results for extended states ( $V_2 = 0.9$ ) are shown in panel [a] and the results for critical states ( $V_2 = 1.1$ ) in panel [b].

### APPENDIX C: DERIVATION AND COMPUTATION OF THE OPTICAL CONDUCTIVITY WITH BAND PROJECTION

The optical conductivity is a linear response function that relates the current ( $J$ ) to a transverse electric field ( $E$ ) [70]:

$$J(\omega) = \sigma(\omega)E_{\perp}(\omega). \quad (\text{C1})$$

The real part of the optical conductivity ( $\sigma'$ ) is associated with the energy absorption from the electric field, while the imaginary part ( $\sigma''$ ) represents the phase shift between the current and the applied field, typical of phenomena such as polarization and inductance. These terms are related by a Kramers-Kronig relation:

$$\sigma''(\omega) = \int_{-\infty}^{\infty} \frac{d\omega'}{\pi} \mathcal{P} \frac{\sigma'(\omega')}{\omega - \omega'}, \quad (\text{C2})$$

where  $\mathcal{P}$  is the Cauchy principal value of the integral. In general, one may write [71]:

$$\sigma(\omega) = \frac{iD}{\omega + i\eta} + \sigma_{reg}(\omega), \quad (\text{C3})$$

where  $D$  is the Drude weight and  $\sigma_{reg}(\omega)$  is the regular part of the optical conductivity, excluding the singular contribution at  $\omega = 0$ .

The Drude weight quantifies the response of free electrons to an applied electric field [72]. It can be used to characterize ballistic transport and, more broadly, to identify Mott transitions. For systems with discrete translational symmetry,  $D$  can serve as an order parameter:  $D \neq 0$  for metallic ground states and  $D = 0$  for non-metallic ground states [70].

The Drude weight can be conveniently expressed in terms of a static vector field ( $A$ ) [70, 71]:

$$D = \frac{1}{N} \left. \frac{\partial^2 E_{g.s.}}{\partial A^2} \right|_{A=0} \quad (\text{C4})$$

For lattice model calculations, we write the Drude weight as:

$$D = \frac{1}{N} \left[ \langle -T \rangle_0 - 2 \sum_{\nu \neq 0} \frac{|\langle \nu | J | 0 \rangle|^2}{E_{\nu} - E_0} \right], \quad (\text{C5})$$

where  $T$  and  $J$  are the current and kinetic energy operators, respectively given by:

$$T = - \sum_{r=0}^{N-1} t_r (c_r^{\dagger} c_{r+1} + c_{r+1}^{\dagger} c_r), \quad (\text{C6})$$

$$J = \left. \frac{\partial H}{\partial A} \right|_{A=0} = -i \sum_{r=0}^{N-1} t_r (c_r^{\dagger} c_{r+1} - c_{r+1}^{\dagger} c_r), \quad (\text{C7})$$

and  $t_r = 1 + V \cos[2\pi\tau(r + 1/2) + \phi]$  is the hopping of our flatband 1D Hamiltonian, given by Eq. 1 in the main text.

Equation C5 can be obtained as follows: (i) couple the model to an electromagnetic field via the Peierls substitution,  $t_r \rightarrow t_r e^{i\mathbf{A}}$ ; (ii) expand the Peierls phase up to second order,  $e^{i\mathbf{A}} \simeq 1 + i\mathbf{A} - \mathbf{A}^2/2$ ; (iii) expand the energy shift between the ground states with and without the vector field ( $\mathbf{A}$ ),  $\Delta E_{g.s.} = E_0(\mathbf{A}) - E_0(0)$ , up to second order; (iv) compute  $\Delta E_{g.s.}$  using second-order perturbation theory.

To obtain the optical conductivity, we start with the Kubo formula:

$$\langle J_{total} \rangle(t) = \frac{1}{N} \left[ \langle T \rangle_0 A(t) + \int dt' \Pi(t, t') A(t') \right], \quad (\text{C8})$$

where the current-current correlation function is:

$$\Pi(t, t') = -i\Theta(t - t') \langle [J(t), J(t')] \rangle, \quad (\text{C9})$$

and the step function,  $\Theta(t - t')$ , ensures causality.

In the Lehmann representation, we write:

$$\begin{aligned}\Pi(t, t') &= -i\Theta(t-t') \frac{1}{Z} \sum_{\alpha, \beta} (e^{-\beta E_\alpha} - e^{-\beta E_\beta}) e^{i(E_\alpha - E_\beta)(t-t')} J_{\alpha\beta} J_{\beta\alpha} \\ \Pi(t, t') &= -i\Theta(t-t') \frac{1}{Z} \sum_{\alpha \neq \beta} (e^{-\beta E_\alpha} - e^{-\beta E_\beta}) e^{i(E_\alpha - E_\beta)(t-t')} J_{\alpha\beta} J_{\beta\alpha},\end{aligned}\tag{C10}$$

where  $J_{\alpha\beta} = \langle \alpha | J | \beta \rangle$ . Notice that when  $\alpha = \beta$ ,  $\Pi(t, t') = 0$  due to the term  $(e^{-\beta E_\alpha} - e^{-\beta E_\beta})$ , since  $J_{\alpha\alpha}$  is finite.

To move to the frequency domain, we perform a Fourier transform:

$$\Pi(\omega) = \int_0^\infty dt e^{i\omega t} \Pi(t, 0).\tag{C11}$$

Using the integral representation of the step function:

$$\Theta(t) = - \int_{-\infty}^\infty \frac{d\omega'}{2\pi i} \frac{e^{-i\omega' t}}{\omega' + i\eta},\tag{C12}$$

we find:

$$\begin{aligned}\int_0^\infty dt e^{i\omega t} \Theta(t) e^{i(E_\alpha - E_\beta)t} &= - \int_0^\infty dt e^{i\omega t} e^{i(E_\alpha - E_\beta)t} \int_{-\infty}^\infty \frac{d\omega'}{2\pi i} \frac{e^{-i\omega' t}}{\omega' + i\eta} \\ &= i \int_{-\infty}^\infty \frac{d\omega'}{\omega' + i\eta} \int_0^\infty \frac{dt}{2\pi} e^{i(\omega + E_\alpha - E_\beta - \omega')t} \\ &= i \int_{-\infty}^\infty \frac{d\omega'}{\omega' + i\eta} \delta(\omega + E_\alpha - E_\beta - \omega') = i \frac{1}{\omega + E_\alpha - E_\beta + i\eta}.\end{aligned}\tag{C13}$$

This representation of the step function naturally introduces the infinitesimal term  $i\eta$  avoiding the need for *ad hoc* adjustments to ensure convergence of the integral.

Plugging this result into Eq. C11, we have

$$\Pi(\omega) = \frac{1}{Z} \sum_{\alpha \neq \beta} (e^{-\beta E_\alpha} - e^{-\beta E_\beta}) \frac{J_{\alpha\beta} J_{\beta\alpha}}{\omega + E_\alpha - E_\beta + i\eta}.\tag{C14}$$

At zero temperature, the nonzero contributions arise when  $|\alpha\rangle$  corresponds to the ground state and  $|\beta\rangle$  to the excited states or vice-versa. Therefore, we have

$$\begin{cases} \frac{(e^{-\beta E_\alpha} - e^{-\beta E_\beta})}{Z} = 1 & \text{if } |\alpha\rangle = |0\rangle, \\ \frac{(e^{-\beta E_\alpha} - e^{-\beta E_\beta})}{Z} = -1 & \text{if } |\beta\rangle = |0\rangle, \end{cases}\tag{C15}$$

Substituting this into Eq. C14 gives us the current-current correlation function at  $T = 0$ :

$$\begin{aligned}\Pi(\omega) &= \sum_{\nu \neq 0} \frac{J_{0\nu} J_{\nu 0}}{\omega + E_0 - E_\nu + i\eta} - \frac{J_{0\nu} J_{\nu 0}}{\omega - E_0 + E_\nu + i\eta} \\ &= \sum_{\nu \neq 0} \frac{J_{0\nu} J_{\nu 0}}{\omega - \Delta E_0^\nu + i\eta} - \frac{J_{0\nu} J_{\nu 0}}{\omega + \Delta E_0^\nu + i\eta},\end{aligned}\tag{C16}$$

where  $\Delta E_0^\nu = E_\nu - E_0$ .

Therefore, Eq. C8 becomes:

$$\langle J_{total} \rangle(\omega) = \frac{1}{N} [ \langle T \rangle_0 + \Pi(\omega) ] \mathbf{A}(\omega).\tag{C17}$$

The conductivity in the frequency domain is defined as:

$$\langle J_{total} \rangle(\omega) = \sigma(\omega) \mathbf{E}(\omega),\tag{C18}$$

where  $\mathbf{E}(\omega) = -i(\omega + i\eta) \mathbf{A}(\omega)$ . Substituting Eq. C18 into Eq. C13:

$$\begin{aligned}\sigma(\omega) i(\omega + i\eta) &= \frac{1}{N} [ \langle T \rangle_0 + \Pi(\omega) ], \\ \leftrightarrow \sigma(\omega) &= \frac{i}{\omega + i\eta} \left[ \frac{\langle -T \rangle_0}{N} + \frac{1}{N} \sum_{\nu \neq 0} \frac{|\langle \nu | J | 0 \rangle|^2}{\omega - \Delta E_0^\nu + i\eta} \right. \\ &\quad \left. - \frac{1}{N} \sum_{\nu \neq 0} \frac{|\langle \nu | J | 0 \rangle|^2}{\omega + \Delta E_0^\nu + i\eta} \right].\end{aligned}\tag{C19}$$

To express the optical conductivity in terms of the Drude weight and its regular part, we combine Eqs. C5 and C19 to get

$$\begin{aligned}\sigma(\omega) &= \frac{i}{\omega + i\eta} \left[ D + \frac{2}{N} \sum_{\nu \neq 0} \frac{|\langle \nu | J | 0 \rangle|^2}{\Delta E_0^\nu} \right. \\ &\quad \left. + \frac{1}{N} \sum_{\nu \neq 0} \frac{|\langle \nu | J | 0 \rangle|^2}{\omega - \Delta E_0^\nu + i\eta} - \frac{1}{N} \sum_{\nu \neq 0} \frac{|\langle \nu | J | 0 \rangle|^2}{\omega + \Delta E_0^\nu + i\eta} \right], \\ \sigma(\omega) &= \frac{iD}{\omega + i\eta} + \sigma_{reg}(\omega),\end{aligned}\tag{C20}$$

thereby recovering Eq. C3, where the regular part of the optical conductivity is given by:

$$\sigma_{reg}(\omega) = \frac{i}{\omega + i\eta} \left[ \frac{2}{N} \sum_{\nu \neq 0} \frac{|\langle \nu | J | 0 \rangle|^2}{\Delta E_0^\nu} + \frac{1}{N} \sum_{\nu \neq 0} \frac{|\langle \nu | J | 0 \rangle|^2}{\omega - \Delta E_0^\nu + i\eta} - \frac{1}{N} \sum_{\nu \neq 0} \frac{|\langle \nu | J | 0 \rangle|^2}{\omega + \Delta E_0^\nu + i\eta} \right]. \quad (\text{C21})$$

It is important to note that  $\lim_{\omega \rightarrow 0} \sigma_{reg}(\omega) \simeq \pi \delta(\omega) \times 0 = 0$ , if we take  $\eta^2 \simeq 0$ . This result is expected for systems with discrete translation invariance at zero temperature, but may not hold when translational symmetry is broken [56].

To extract the real part of the optical conductivity, we first manipulate the complex prefactor on the right-hand side of Eq. C21 to separate its real and imaginary parts:

$$\frac{i}{\omega + i\eta} = \frac{i(\omega - i\eta)}{(\omega + i\eta)(\omega - i\eta)} = \frac{i\omega + \eta}{\omega^2 + \eta^2}. \quad (\text{C22})$$

We apply the same procedure to the middle term in the right-hand side of Eq.C21:

$$\frac{|\langle \nu | J | 0 \rangle|^2}{\omega - \Delta E_0^\nu + i\eta} = \frac{|\langle \nu | J | 0 \rangle|^2 (\omega - \Delta E_0^\nu - i\eta)}{(\omega - \Delta E_0^\nu)^2 + \eta^2}. \quad (\text{C23})$$

Analogously, for the last term:

$$\frac{|\langle \nu | J | 0 \rangle|^2}{\omega + \Delta E_0^\nu + i\eta} = \frac{|\langle \nu | J | 0 \rangle|^2 (\omega + \Delta E_0^\nu - i\eta)}{(\omega + \Delta E_0^\nu)^2 + \eta^2}. \quad (\text{C24})$$

Substituting Eqs. C22, C23, C24 into Eq. C21, we get:

$$\sigma_{reg}(\omega) = \frac{i\omega + \eta}{\omega^2 + \eta^2} \left[ \frac{2}{N} \sum_{\nu \neq 0} \frac{|\langle \nu | J | 0 \rangle|^2}{\Delta E_0^\nu} + \frac{1}{N} \sum_{\nu \neq 0} \frac{|\langle \nu | J | 0 \rangle|^2 (\omega - \Delta E_0^\nu - i\eta)}{(\omega - \Delta E_0^\nu)^2 + \eta^2} \right. \quad (\text{C25})$$

$$\left. - \frac{1}{N} \sum_{\nu \neq 0} \frac{|\langle \nu | J | 0 \rangle|^2 (\omega + \Delta E_0^\nu - i\eta)}{(\omega + \Delta E_0^\nu)^2 + \eta^2} \right]. \quad (\text{C26})$$

The real part of Eq.C26 is straightforward to derive and is given by:

$$\Re[\sigma_{reg}(\omega)] = \frac{\eta}{\omega^2 + \eta^2} \frac{2}{N} \sum_{\nu \neq 0} \frac{|\langle \nu | J | 0 \rangle|^2}{\Delta E_0^\nu} + \frac{1}{\omega^2 + \eta^2} \frac{1}{N} \sum_{\nu \neq 0} |\langle \nu | J | 0 \rangle|^2 \left[ (\omega - \Delta E_0^\nu) L_{(\omega, \Delta E_0^\nu, \eta)}^+ - (\omega + \Delta E_0^\nu) L_{(\omega, \Delta E_0^\nu, \eta)}^- \right] + \frac{\omega}{\omega^2 + \eta^2} \frac{1}{N} \sum_{\nu \neq 0} |\langle \nu | J | 0 \rangle|^2 \left[ L_{(\omega, \Delta E_0^\nu, \eta)}^+ - L_{(\omega, \Delta E_0^\nu, \eta)}^- \right], \quad (\text{C27})$$

where the Lorentzian terms are:

$$L_{(\omega, \Delta E_0^\nu, \eta)}^+ = \frac{\eta}{(\omega - \Delta E_0^\nu)^2 + \eta^2}, \quad (\text{C28})$$

$$L_{(\omega, \Delta E_0^\nu, \eta)}^- = \frac{\eta}{(\omega + \Delta E_0^\nu)^2 + \eta^2}. \quad (\text{C29})$$

Explicitly taking the limit  $\eta \rightarrow 0$ , we have:

$$\begin{aligned} \Re[\sigma_{reg}(\omega)] &= \frac{\pi}{N} \sum_{\nu \neq 0} \frac{|\langle \nu | J | 0 \rangle|^2}{\omega^2} \left[ (\omega - \Delta E_0^\nu) \delta_{(\omega - \Delta E_0^\nu)} \right. \\ &\quad \left. - (\omega + \Delta E_0^\nu) \delta_{(\omega + \Delta E_0^\nu)} \right] \\ &\quad + \frac{\pi}{N} \sum_{\nu \neq 0} \frac{|\langle \nu | J | 0 \rangle|^2}{\omega} \left[ \delta_{(\omega - \Delta E_0^\nu)} - \delta_{(\omega + \Delta E_0^\nu)} \right], \\ &= \frac{\pi}{N} \sum_{\nu \neq 0} \frac{|\langle \nu | J | 0 \rangle|^2}{\omega} \left[ \delta_{(\omega - \Delta E_0^\nu)} - \delta_{(\omega + \Delta E_0^\nu)} \right], \\ &= \frac{\pi}{N} \sum_{\nu \neq 0} \frac{|\langle \nu | J | 0 \rangle|^2}{\Delta E_0^\nu} \delta_{(|\omega| - \Delta E_0^\nu)}. \end{aligned} \quad (\text{C30})$$

The first two terms in the first line of Eq. C30 are null since  $x\delta(x) = 0$ .

Eq. C30 exhibits a symmetric structure with respect to  $\omega$ . Given that  $E_0^\nu > 0$ , the first delta function in the second-to-last line of Eq. C30 is localized only for positive values of  $\omega$ , while the second delta function

is localized for negative values. In the last line, the equation is presented in a form commonly found in the

literature[52, 55].

The term  $|\langle \nu | J | 0 \rangle|^2$  in Eq. C30 can be written in terms of the FB operators as

$$\begin{aligned}
 |\langle \nu | J | 0 \rangle|^2 &= \langle 0 | \sum_{j,k \in FB} -i \sum_{r=0}^{N-1} t_r [\langle j | r \rangle \langle r+1 | k \rangle - \langle j | r+1 \rangle \langle r | k \rangle] d_j^\dagger d_k | \nu \rangle \\
 &\times \langle \nu | i \sum_{l,m \in FB} t_r [\langle l | r+1 \rangle \langle r | m \rangle - \langle l | r \rangle \langle r+1 | m \rangle] d_l^\dagger d_m | 0 \rangle.
 \end{aligned}
 \tag{C31}$$

## APPENDIX D: FIRST-ORDER PERTURBATION THEORY RESULTS

Below we show the results for the fidelity susceptibility, the charge gap and the IPR of the average of the density fluctuations in momentum space using first order band projection, given by Eq. 3, for  $V_2 = 0.9$ . As we can see in Fig. D1(a)-(c), no transition is captured. The results for  $\Delta_C$  and  $IPR_K(\langle \delta \mathbf{n} \rangle)$  indicate that, even when increasing interactions, we still remain in the LL phase. The results contrast drastically with those of Fig. 3(a)-(c), where we used band projection up to second order.

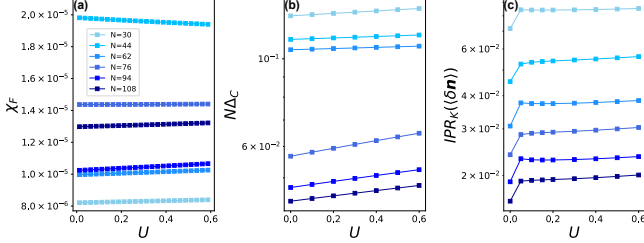


FIG. D1. First order band projection for the computations of: (a) the fidelity susceptibility ( $\chi_F$ ), defined by Eq. 6 with  $\delta U = 1.25 \times 10^{-2}$ ; (b) the charge gap ( $\Delta_C$ ), defined by Eq. 7; (c) the IPR of the average of the density fluctuations in momentum space ( $IPR_K(\langle \delta \mathbf{n} \rangle)$ ), defined by Eq. 8. Results are averaged over 10 random configurations of  $\phi$  and  $\theta$ .

We also compare the results for  $\chi_F, \Delta_C$  and  $IPR_K(\langle \delta \mathbf{n} \rangle)$ , Fig. D2(a)-(c), using first-order BP (light blue curves), BP up to second order (blue curves) and first-order terms with the most relevant second-order term (dark blue curves), corresponding to the Feynman Diagrams (a), (b) and (j) in Fig. 2. The second-order contribution is a two-body term in the FB subspace, involving contributions from all bands.

As can be seen in Fig. D2, the results for (a)+(b)+(j) capture the relevant Physics of the model and are very close to those from BP up to second order.

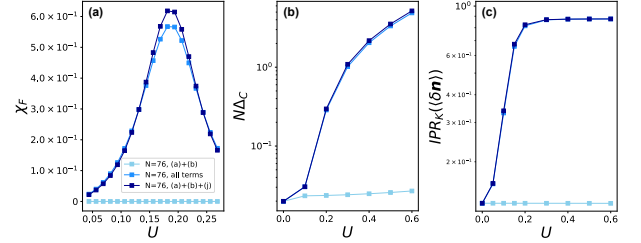


FIG. D2. Computation of (a) the fidelity susceptibility ( $\chi_F$ ), defined by Eq. 6 with  $\delta U = 1.25 \times 10^{-2}$ ; (b) the charge gap ( $\Delta_C$ ), defined by Eq. 7; (c) the IPR of the average of the density fluctuations in momentum space ( $IPR_K(\langle \delta \mathbf{n} \rangle)$ ), defined by Eq. 8, using first-order BP, BP up to second-order and first-order terms plus the most relevant second-order term, for  $N = 76$ ,  $V_2 = 0.9$ .

- [1] Serge Aubry and Gilles André. Analyticity breaking and Anderson localization in incommensurate lattices. *Ann. Israel Phys. Soc.*, 3(133):18, 1980.
- [2] JH Pixley, Justin H Wilson, David A Huse, and Sarang Gopalakrishnan. Weyl semimetal to metal phase transitions driven by quasiperiodic potentials. *Physical review letters*, 120(20):207604, 2018.
- [3] Yixing Fu, Elio J König, Justin H Wilson, Yang-Zhi Chou, and Jediah H Pixley. Magic-angle semimetals. *Quantum Materials*, 5(1):1–8, 2020.
- [4] Miguel Gonçalves, Hadi Z. Olyaei, Bruno Amorim, Rubem Mondaini, Pedro Ribeiro, and Eduardo V. Castro. Incommensurability-induced sub-ballistic narrow-band-states in twisted bilayer graphene. *2D Materials*, 9(1):011001, jan 2022. ISSN 2053-1583. doi: 10.1088/2053-1583/ac3259. URL <https://iopscience.iop.org/article/10.1088/2053-1583/ac3259>.
- [5] Hepeng Yao, Hakim Khoudli, Léa Bresque, and Laurent Sanchez-Palencia. Critical behavior and fractality in shallow one-dimensional quasiperiodic potentials. *Physical review letters*, 123(7):070405, 2019.
- [6] Biao Huang and W Vincent Liu. Moiré localization in two-dimensional quasiperiodic systems. *Physical Review B*, 100(14):144202, 2019.
- [7] Michael Schreiber, Sean S Hodgman, Pranjal Bordia, Henrik P Lüschen, Mark H Fischer, Ronen Vosk, Ehud

- Altman, Ulrich Schneider, and Immanuel Bloch. Observation of many-body localization of interacting fermions in a quasirandom optical lattice. *Science*, 349(6250):842–845, 2015.
- [8] Miguel Gonçalves, Bruno Amorim, Eduardo V Castro, and Pedro Ribeiro. Critical phase dualities in 1d exactly solvable quasiperiodic models. *Physical Review Letters*, 131(18):186303, 2023.
- [9] Miguel Gonçalves, Bruno Amorim, Eduardo V. Castro, and Pedro Ribeiro. Renormalization group theory of one-dimensional quasiperiodic lattice models with commensurate approximants. *Physical Review B*, 108(10):L100201, sep 2023. ISSN 2469-9950. doi: 10.1103/PhysRevB.108.L100201. URL <https://link.aps.org/doi/10.1103/PhysRevB.108.L100201>.
- [10] Fangli Liu, Somnath Ghosh, and YD Chong. Localization and adiabatic pumping in a generalized aubry-andré-harper model. *Physical Review B*, 91(1):014108, 2015.
- [11] Tong Liu, Xu Xia, Stefano Longhi, and Laurent Sanchez-Palencia. Anomalous mobility edges in one-dimensional quasiperiodic models. *SciPost Physics*, 12(1):027, 2022.
- [12] Yucheng Wang, Chen Cheng, Xiong-Jun Liu, and Dapeng Yu. Many-body critical phase: extended and nonthermal. *Physical Review Letters*, 126(8):080602, 2021.
- [13] Yucheng Wang, Long Zhang, Sen Niu, Dapeng Yu, and Xiong-Jun Liu. Realization and detection of nonergodic critical phases in an optical raman lattice. *Physical Review Letters*, 125(7):073204, 2020.
- [14] Yoav Lahini, Rami Pugatch, Francesca Pozzi, Marc Sorel, Roberto Morandotti, Nir Davidson, and Yaron Silberberg. Observation of a localization transition in quasiperiodic photonic lattices. *Physical review letters*, 103(1):013901, 2009.
- [15] Dimitrii Tanese, Evgeni Gurevich, Florent Baboux, Thibaut Jacqmin, Aristide Lemaître, Elisabeth Galopin, Isabelle Sagnes, Alberto Amo, Jacqueline Bloch, and Eric Akkermans. Fractal energy spectrum of a polariton gas in a fibonacci quasiperiodic potential. *Physical review letters*, 112(14):146404, 2014.
- [16] Kevin Singh, Kush Saha, Siddharth A Parameswaran, and David M Weld. Fibonacci optical lattices for tunable quantum quasicrystals. *Physical Review A*, 92(6):063426, 2015.
- [17] Thomas Kohlert, Sebastian Scherg, Xiao Li, Henrik P Lüschen, Sankar Das Sarma, Immanuel Bloch, and Monika Aidelsburger. Observation of many-body localization in a one-dimensional system with a single-particle mobility edge. *Physical review letters*, 122(17):170403, 2019.
- [18] Fangzhao Alex An, Karmela Padavić, Eric J. Meier, Suraj Hegde, Sriram Ganeshan, J. H. Pixley, Smitha Vishveshwara, and Bryce Gadway. Interactions and Mobility Edges: Observing the Generalized Aubry-André Model. *Physical Review Letters*, 126(4):040603, jan 2021. ISSN 0031-9007. doi: 10.1103/PhysRevLett.126.040603. URL <https://link.aps.org/doi/10.1103/PhysRevLett.126.040603>.
- [19] Miguel Gonçalves. Entanglement entropy scaling in critical phases of one-dimensional quasiperiodic systems. *Physical Review B*, 109(10):104202, 2024.
- [20] Sriram Ganeshan, JH Pixley, and S Das Sarma. Nearest neighbor tight binding models with an exact mobility edge in one dimension. *Physical review letters*, 114(14):146601, 2015.
- [21] Pedro Ribeiro, Masudul Haque, and Achilleas Lazarides. Strongly interacting bosons in multichromatic potentials supporting mobility edges: Localization, quasi-condensation, and expansion dynamics. *Physical Review A*, 87(4):043635, 2013.
- [22] Yucheng Wang, Xu Xia, Long Zhang, Hepeng Yao, Shu Chen, Jiangong You, Qi Zhou, and Xiong-Jun Liu. One-dimensional quasiperiodic mosaic lattice with exact mobility edges. *Physical Review Letters*, 125(19):196604, 2020.
- [23] J Biddle, DJ Priour Jr, B Wang, and S Das Sarma. Localization in one-dimensional lattices with non-nearest-neighbor hopping: Generalized anderson and aubry-andré models. *Physical Review B*, 83(7):075105, 2011.
- [24] X Deng, S Ray, S Sinha, GV Shlyapnikov, and L Santos. One-dimensional quasicrystals with power-law hopping. *Physical review letters*, 123(2):025301, 2019.
- [25] Miguel Gonçalves, Bruno Amorim, Eduardo Castro, and Pedro Ribeiro. Hidden dualities in 1D quasiperiodic lattice models. *SciPost Physics*, 13(3):046, sep 2022. ISSN 2542-4653. doi: 10.21468/SciPostPhys.13.3.046. URL <https://scipost.org/10.21468/SciPostPhys.13.3.046>.
- [26] Henrik P Lüschen, Sebastian Scherg, Thomas Kohlert, Michael Schreiber, Pranjal Bordia, Xiao Li, S Das Sarma, and Immanuel Bloch. Single-particle mobility edge in a one-dimensional quasiperiodic optical lattice. *Physical review letters*, 120(16):160404, 2018.
- [27] DinhDuy Vu and S Das Sarma. Moiré versus mott: Incommensuration and interaction in one-dimensional bichromatic lattices. *Physical Review Letters*, 126(3):036803, 2021.
- [28] Miguel Gonçalves, Bruno Amorim, Flavio Riche, Eduardo V Castro, and Pedro Ribeiro. Incommensurability enabled quasi-fractal order in 1d narrow-band moiré systems. *Nature Physics*, 20:1933, 2024.
- [29] Miguel Gonçalves, Jedediah H Pixley, Bruno Amorim, Eduardo V Castro, and Pedro Ribeiro. Short-range interactions are irrelevant at the quasiperiodicity-driven luttinger liquid to anderson glass transition. *Physical Review B*, 109(1):014211, 2024.
- [30] Flavio Riche, Miguel Gonçalves, Bruno Amorim, Eduardo V Castro, and Pedro Ribeiro. Fractal quasicondensation in one dimension. *Physical Review B*, 110(22):224523, 2024.
- [31] Hepeng Yao, Luca Tanzi, Laurent Sanchez-Palencia, Thierry Giamarchi, Giovanni Modugno, and Chiara D’errico. Mott transition for a lieb-liniger gas in a shallow quasiperiodic potential: Delocalization induced by disorder. *Physical Review Letters*, 133(12):123401, 2024.
- [32] Chao Zhang. Quasi-solid and supersolid from quasiperiodic long-range interactions. *arXiv preprint arXiv:2511.02218*, 2025.
- [33] Guo-Qing Zhang, Ling-Zhi Tang, LF Quezada, Shi-Hai Dong, and Dan-Wei Zhang. Reentrant topological phases and spin density wave induced by 1d moiré potentials. *Communications Physics*, 8(1):275, 2025.
- [34] Yang-Zhi Chou, Yixing Fu, Justin H Wilson, EJ König, and JH Pixley. Magic-angle semimetals with chiral symmetry. *Physical Review B*, 101(23):235121, 2020.
- [35] Steven M Girvin and Kun Yang. *Modern condensed matter physics*. Cambridge University Press, 2019.
- [36] Eva Y Andrei and Allan H MacDonald. Graphene bi-

- layers with a twist. *Nature materials*, 19(12):1265–1275, 2020.
- [37] Bohao Li, Wen-Xuan Qiu, Fengcheng Wu, and AH MacDonald. Quantum phases in twisted homobilayer transition metal dichalcogenides. *arXiv preprint arXiv:2509.07360*, 2025.
- [38] Chonghao Wang, Xiaoyang Shen, Ruiping Guo, Wenhui Duan, Chong Wang, and Yong Xu. Fractional chern insulators in moiré flat bands with high chern numbers. *Physical Review B*, 112(20):L201109, 2025.
- [39] Zhao Liu, Emil J Bergholtz, Heng Fan, and Andreas M Läuchli. Fractional chern insulators in topological flat bands with higher chern number. *Physical review letters*, 109(18):186805, 2012.
- [40] Titus Neupert, Luiz Santos, Claudio Chamon, and Christopher Mudry. Fractional quantum hall states at zero magnetic field. *Physical review letters*, 106(23):236804, 2011.
- [41] Emil J Bergholtz and Zhao Liu. Topological flat band models and fractional chern insulators. *International Journal of Modern Physics B*, 27(24):1330017, 2013.
- [42] Inti Sodemann and AH MacDonald. Landau level mixing and the fractional quantum hall effect. *Physical Review B*, 87(24):245425, 2013.
- [43] Loïc Herviou and Frédéric Mila. Possible restoration of particle-hole symmetry in the 5/2-quantized hall state at small magnetic field. *Physical Review B*, 107(11):115137, 2023.
- [44] Yujin Jia, Jiabin Yu, Jiaxuan Liu, Jonah Herzog-Arbeitman, Ziyue Qi, Hanqi Pi, Nicolas Regnault, Hongming Weng, B Andrei Bernevig, and Quansheng Wu. Moiré fractional chern insulators. i. first-principles calculations and continuum models of twisted bilayer mote 2. *Physical Review B*, 109(20):205121, 2024.
- [45] Jiabin Yu, Jonah Herzog-Arbeitman, Minxuan Wang, Oskar Vafeek, B Andrei Bernevig, and Nicolas Regnault. Fractional chern insulators versus nonmagnetic states in twisted bilayer mote 2. *Physical Review B*, 109(4):045147, 2024.
- [46] Jiabin Yu, Jonah Herzog-Arbeitman, Yves H Kwan, Nicolas Regnault, and B Andrei Bernevig. Moiré fractional chern insulators. iv. fluctuation-driven collapse in multiband exact diagonalization calculations on rhombohedral graphene. *Physical Review B*, 112(7):075110, 2025.
- [47] Ahmed Abouelkomsan, Aidan P Reddy, Liang Fu, and Emil J Bergholtz. Band mixing in the quantum anomalous hall regime of twisted semiconductor bilayers. *Physical Review B*, 109(12):L121107, 2024.
- [48] Cheng Xu, Jiangxu Li, Yong Xu, Zhen Bi, and Yang Zhang. Maximally localized wannier functions, interaction models, and fractional quantum anomalous hall effect in twisted bilayer mote2. *Proceedings of the National Academy of Sciences*, 121(8):e2316749121, 2024.
- [49] Heqiu Li, B Andrei Bernevig, and Nicolas Regnault. Multiband exact diagonalization and an iteration approach to search for fractional chern insulators in rhombohedral multilayer graphene. *Physical Review B*, 112(7):075130, 2025.
- [50] Xiaoyang Shen, Chonghao Wang, Ruiping Guo, Zhiming Xu, Wenhui Duan, and Yong Xu. Stabilizing fractional chern insulators via exchange interaction in moiré systems. *arXiv preprint arXiv:2405.12294*, 2024.
- [51] Shi-Jian Gu. Fidelity approach to quantum phase transitions. *International Journal of Modern Physics B*, 24(23):4371–4458, 2010.
- [52] B Sriram Shastry and Bill Sutherland. Twisted boundary conditions and effective mass in heisenberg-ising and hubbard rings. *Physical review letters*, 65(2):243, 1990.
- [53] CA Stafford, AJ Millis, and BS Shastry. Finite-size effects on the optical conductivity of a half-filled hubbard ring. *Physical Review B*, 43(16):13660, 1991.
- [54] CA Stafford and AJ Millis. Scaling theory of the mott-hubbard metal-insulator transition in one dimension. *Physical Review B*, 48(3):1409, 1993.
- [55] RM Fye, MJ Martins, DJ Scalapino, J Wagner, and W Hanke. Drude weight, optical conductivity, and flux properties of one-dimensional hubbard rings. *Physical Review B*, 44(13):6909, 1991.
- [56] AJ Millis and SN Coppersmith. Interaction and doping dependence of optical spectral weight of the two-dimensional hubbard model. *Physical Review B*, 42(16):10807, 1990.
- [57] Adriana Moreo and Elbio Dagotto. Optical conductivity of the hubbard and t-j models. *Physical Review B*, 42(7):4786, 1990.
- [58] Can Shao, Hao Yuan, and Ruifeng Lu. Using optical conductivity to detect the underlying metallic edge state in the interacting haldane model. *Physical Review B*, 104(11):115146, 2021.
- [59] Siddharth A Parameswaran, Rahul Roy, and Shivaji L Sondhi. Fractional quantum hall physics in topological flat bands. *Comptes Rendus Physique*, 14(9-10):816–839, 2013.
- [60] Ke Huang, Xiao Li, Sankar Das Sarma, and Fan Zhang. Self-consistent theory of fractional quantum anomalous hall states in rhombohedral graphene. *Physical Review B*, 110(11):115146, 2024.
- [61] Zuzhang Lin, Hongyu Lu, Wenqi Yang, Dawei Zhai, and Wang Yao. Fractional chern insulator states in an isolated flat band of zero chern number. *Newton*, 2025.
- [62] Xiao-Liang Qi. Generic wave-function description of fractional quantum anomalous hall states? format? and fractional topological insulators. *Physical review letters*, 107(12):126803, 2011.
- [63] Miguel Angel Cazalilla, Roberta Citro, Thierry Giamarchi, Edmond Orignac, and Marcos Rigol. One dimensional bosons: From condensed matter systems to ultracold gases. *Reviews of Modern Physics*, 83(4):1405–1466, 2011.
- [64] T Giamarchi and AJ Millis. Conductivity of a luttinger liquid. *Physical Review B*, 46(15):9325, 1992.
- [65] Xuanbo Feng, Jans Henke, Corentin Morice, Charles J Sayers, Enrico Da Como, Jasper Van Wezel, and Erik Van Heumen. Signatures of the charge density wave collective mode in the infrared optical response of vse 2. *Physical Review B*, 104(16):165134, 2021.
- [66] Holger Fehske and Eric Jeckelmann. Quantum phase transitions in one-dimensional electron-phonon systems. In *Polarons in Bulk Materials and Systems With Reduced Dimensionality*, pages 297–311. IOS Press, 2006.
- [67] Li-Qiao Xia, Aviram Uri, Jiaojie Yan, Aaron Sharpe, Filippo Gaggioli, Nicole S Ticea, Julian May-Mann, Kenji Watanabe, Takashi Taniguchi, Liang Fu, et al. Magic continuum in multi-moiré twisted trilayer graphene. *arXiv preprint arXiv:2509.03583*, 2025.
- [68] Aviram Uri, Sergio C de la Barrera, Mallika T Randeria, Daniel Rodan-Legrain, Trithep Devakul, Philip JD Crow-

- ley, Nisarga Paul, Kenji Watanabe, Takashi Taniguchi, Ron Lifshitz, et al. Superconductivity and strong interactions in a tunable moiré quasicrystal. *Nature*, 620 (7975):762–767, 2023.
- [69] Xinyuan Lai, Guohong Li, Angela M Coe, Jedediah H Pixley, Kenji Watanabe, Takashi Taniguchi, and Eva Y Andrei. Moiré periodic and quasiperiodic crystals in heterostructures of twisted bilayer graphene on hexagonal boron nitride. *Nature materials*, pages 1–8, 2025.
- [70] AJ Millis. Optical conductivity and correlated electron physics. In *Strong interactions in low dimensions*, pages 195–235. Springer, 2004.
- [71] S Kirchner, HG Evertz, and W Hanke. Transport properties of one-dimensional hubbard models. *Physical Review B*, 59(3):1825, 1999.
- [72] Kazuaki Takasan, Masaki Oshikawa, and Haruki Watanabe. Drude weights in one-dimensional systems with a single defect. *Physical Review B*, 107(7):075141, 2023.